Long Baseline Bistatic Radar for Space Situational Awareness

Sarah Welch[1], Gregory Hogan[1], Delphine Cerutti-Maori[2], Simon Garrington[3], Robert Morrison[1], Matern Otten[4], Cees Bassa[5], Nick Pallecaros[6], Philip van Dorp[4], Paul Harrison[6], Tonino Pisanu[7] , Marco Martorella[8],

[1] MIT Lincoln Laboratory, UNITED STATES; [2 4]Fraunhofer FHR, GERMANY; [3]Univ. of Manchester, UNITED KINGDOM; [4]TNO, NETHERLAND; [5]ASTRON Netherlands Institute for Radio Astronomy, NETHERLAND; [6]Dstl, UNITED KINGDOM; [7]INAF, ITALY, [8]Univeristy of Pisa and CNIT, ITALY

swelch@ll.mit.edu
hogan@ll.mit.edu

delphine.cerutti-maori@fhr.fraunhofer.de

simon.garrington@manchester.ac.uk
rmorrison@ll.mit.edu

matern.otten@tno.nl
bassa@astron.nl

ngpallecaros@mail.dstl.gov.uk

philip.vandorp@tno.nl

paul.harrison@manchester.ac.uk

tonino.pisanu@inaf.it

marco.martorella@iet.unipi.it

ABSTRACT

Radar detection and tracking of resident space objects in Geosynchronous (GEO) orbits is challenging due to the loss in sensitivity at the extreme distance of 36,000 km and because of the proliferation of small satellites with decreased radar cross section. One option to increase sensitivity of existing monostatic radar sensors is to employ large aperture radio telescopes configured as bistatic receivers. Moreover, multiple receivers would enable a multi-bistatic configuration with additional performance improvement in terms of both detection and tracking. In this paper we report on long baseline bistatic measurements using the Millstone Hill Radar (MHR) in the USA and the Tracking and Imaging Radar (TIRA) in Germany as transmitters and a number of receivers in Europe: the Sardinia Radio Telescope (SRT) in Italy, the Westerbork Synthesis Radio Telescope (WSRT) in the Netherlands and multiple antennas of the e-MERLIN array in the United Kingdom. The work here presented has been carried out as part of the Program of Work of the SET-293 Research Task Group (RTG).

1.0 INTRODUCTION

The most significant challenge to maintaining Space Situational Awareness (SSA) at Geosynchronous Earth Orbit (GEO) with radar is loss of sensitivity due to extreme distance, which is 36,000 km to the GEO belt. To increase the sensitivity of a monostatic radar, one must increase the transmit power, build a larger aperture, or reduce the system temperature of the sensor. The sensitivity is most affected by the aperture size, as sensitivity scales with the fourth power of the aperture diameter, but it is cost prohibitive to build large aperture radars, and engineering challenges impose an upper limit on the size and slew rate of such sensors

[1]. However, an option to increase sensitivity of existing monostatic sensors is to consider a multistatic radar that uses large aperture radio telescopes as bistatic receivers. There are numerous large diameter (>60 m) radio telescopes that can be paired with radars. Using radio telescopes as receiving elements is advantageous in several ways: in addition to their large size, 1) radio telescopes typically have low system temperatures, often an order of magnitude lower than a radar's, which further increases their sensitivity; 2) their pointing and tracking capabilities are well matched to GEO targets; 3) they are typically equipped with wide-band receivers allowing flexibility to pair with multiple transmitting radars; 4) they usually have excellent frequency standards (H-masers) allowing coherent bistatic observations; and 5) there is potential for combining astronomical and radar observations calibration [2].

While the link budget calculation between such bistatic transmitter/receiver pairs is promising, the bistatic radar cross section (RCS) is a somewhat untested factor, especially over inter-continental baselines. Over shorter baselines, of less than 1000 km, it is likely that the bistatic RCS will be similar to the monostatic RCS, but as even monostatic RCS can be highly directional there will likely be greater variability in bistatic RCS [3]. Moreover, as multiple receiving stations (radiotelescopes) may be available at the same time, multi-bistatic configurations may be enabled that would not only increase the overall system sensitivity and ability to detect objects at GEO but would also improve tracking performances as multi-lateration would help improving both the position and velocity estimation of the object.

In early 2020, NATO Science & Technology Organization (STO) initiated a multi-year Sensors, Electronics and Technology (SET) Research Task Group (RTG) (SET-293) to examine the use of bistatic and multistatic radar configurations for improved SSA of GEO by combining existing NATO partner assets in the USA and Europe. SET-293 has performed experiments to explore real-world limitations to the theoretical link-budget of such bistatic systems. A graphic depicting the radar transmitters (Tx) and receivers (Rx) geometry for the experiments is shown in Figure 1-1.

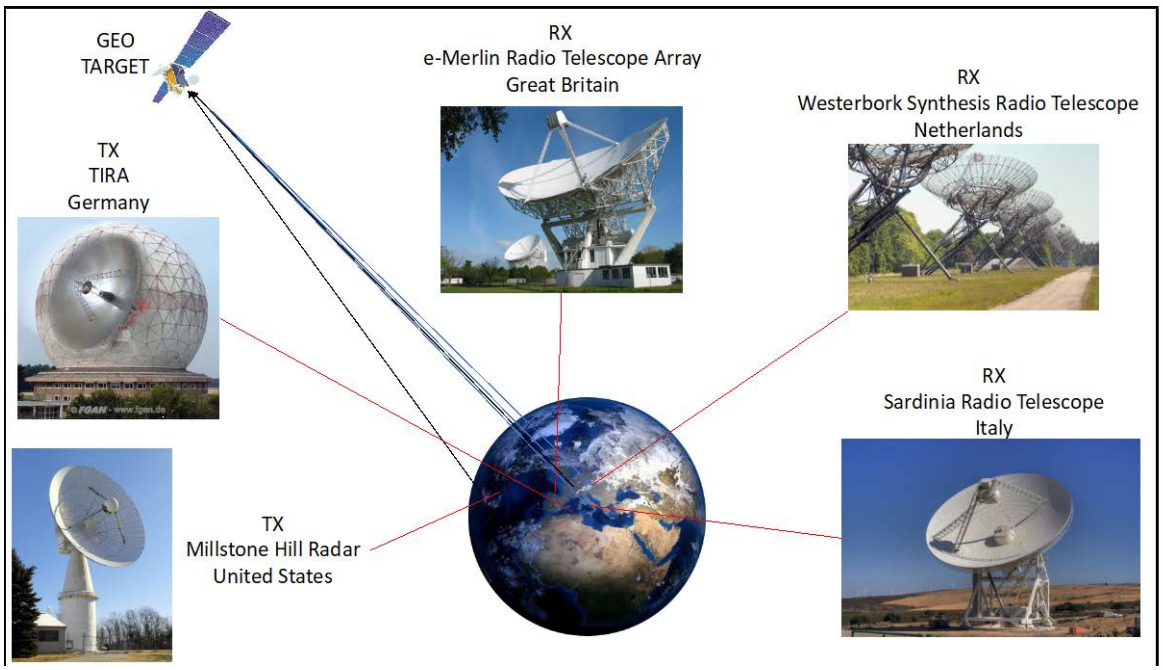

Fig. 1-1 – Radar multistatic experiment geometry depicting the radar transmitters illuminating a Geosynchronous satellite target and the radiotelescope receiving the signal from the satellite.

One set of experiments paired the Millstone Hill Radar (MHR) in the USA with three receivers in Europe: the Sardinia Radio Telescope (SRT) in Italy, a single antenna of the Westerbork Synthesis Radio Telescope (WSRT) in the Netherlands and multiple antennas of the e-MERLIN array, operated by the Jodrell Bank

Observatory (JBO) in the United Kingdom. e-MERLIN comprises 7 antennas with diameters from 25m to 76m and separations from 10km to 220km in the UK, used for high resolution radio astronomy imaging at centimetre wavelengths. The antennas are connected by a dedicated optical network to a central correlator and their coherence is maintained by a two-way RF timing signal on the same fibre. Additional bistatic experiments with smaller baselines were conducted in Europe between TIRA in Germany and the SRT and e-MERLIN radio telescopes. The sensors and their associated parameters are listed in Table 2.1.

The link budget is computed in terms of a Reference SNR for each receiver paired with MHR and TIRA. The reference monostatic SNR is 50 dB for MHR and 47 dB for TIRA, and it describes the maximum performance for a single pulse on a 0 dBsm target at 1000 km range. It is important to note that this link budget calculation assumes that the monostatic and bistatic RCS are equivalent. Additionally, the receiver gain, i.e. the difference between the monostatic sensitivity and the bistatic sensitivity is shown for each of the bistatic receivers in the last row of Table 2.1. The potential benefit of radio telescope receivers is apparent as even the modestly sized WSRT receiver is expected to show nearly 7 dB of receiver gain with MHR and 10 dB gain with TIRA due to its low system temperature as a receive-only system. This paper reports on measurements collected in 2020 and 2021. Additional collections have been conducted in 2022 and will be presented in a future paper.

2.0 PROCESSING OVERVIEW

2.1 Pulse Compression

The Millstone Hill Radar (MHR) is a 25.6 meter L-Band tracking radar located in Westford, Massachusetts in the United States. It is used primarily for deep space surveillance and is a contributing radar to the Space Surveillance Network (SSN) [4]. MHR is a coherent radar, meaning that the phase relationships between pulses are constant, allowing the integration of multiple pulses to increase the SNR. Many satellites are too small for single pulse detection and require coherent pulse integration to increase sensitivity, especially at GEO distances.

Table 2-1 – The sensor parameters and the link budgets are shown for MHR and TIRA monostatically and for each receiver paired with MHR and TIRA. The Reference SNR is the maximum performance on a 0 dBsm target at 1000 km range and is used to compute the RX Gain in the last row, i.e. the improvement in sensitivity of each bistatic receiver over MHR/TIRA monostatically. The WSRT parameters are for a single antenna in the array and two example e-MERLIN antennas are shown

Parameter	MHR	TIRA	e-MERLIN (Lovell)	e-MERLIN (Knockin)	SRT	WSRT
	TX	TX	RX	RX	RX	RX
Lat/Lon (degrees)	42.6, 288.5	50.6 7.1	53.0, 357.4	52.8, 357.0	39.5, 9.2	52.9, 6.6
Antenna Diameter (m)	25.6	34	76	25	64	25
Center Frequency (MHz)	1295	1333	[1250-1750]	[1250-1750]	1295	1295

Ref. SNR (dB)	50	47	66	57	65	57
Rx Gain (dB)	–		16 / 19	7 / 10	15 / 18	7 / 10

MHR operates at a center frequency of 1295 MHz and can transmit linear frequency modulated (LFM) pulses (chirps) up to 8 MHz in bandwidth with a peak power of 3000 kW. Unlike an unmodulated pulse, a chirp's bandwidth allows it to simultaneously have high range resolution and maintain a long enough duration for sufficient SNR [5]. The maximum pulse length is 1 millisecond, and up to 50 pulses can be transmitted per second, though the operating PRF is algorithmically determined based on the waveform and target range to prevent the received pulses from falling within the transmitter guard band.

In order to realize the range resolution and gain of a chirp waveform, the received pulse must undergo a technique known as pulse compression [6]. Once the pulses are compressed, the rest of the signal processing chain, such as coherent integration and target detection, can be executed. Pulse compression is accomplished by matched filtering the received samples with a stored replica of the transmitted pulse, and it is often implemented via a convolution operation. Since the radar cannot receive during the transmit window, it performs a range-gating step ahead of pulse compression by receiving during a small range window. The radar must therefore have an estimate of the target range in order to process the correct delays and detect the target.

The principle of the TIRA system is similar. The radar also operates in L-band at a slightly higher center frequency of 1333 MHz. TIRA uses binary phase shift keyed (BPSK) waveforms as transmit signal. The total pulse length, which is usually 1 millisecond long, is divided into N subpulses. The series of symbols employed to code the phase are arranged in a pseudo random noise sequence. The modulation number N, which ranges from 1 to 250, is set in real-time by the system depending on the SNR of the received signal. To compute the target range and Doppler frequency in real-time, TIRA uses a correlator quartet. The main beam of the ambiguity function is sampled at four distinct points around the expected range/Doppler position of the target (matched filter for different Doppler frequencies and ranges). From these values, the target parameters are estimated. The PRF of the TIRA system is approximately 30 Hz [7-9].

While a bistatic radar system could operate in the same manner, the bistatic experiments of SET-293 are fundamentally very different as the bistatic receivers are completely separate systems with no automated communication between the transmitter and receiver. The receiver must therefore record continuously throughout the duration of the experiment, as the receiver will not know when the transmitted pulses are arriving. The bistatic signal processing must occur offline in a post-processing pipeline.

The main assumption in these experiments is that the target ephemeris is known with reasonable accuracy such that the receiver can use the predicted position to control its pointing and record the transmitted pulses. The target motion is used during post-processing to first extract the receiver samples that contain the pulse, then generate the pulse replica for matched filtering and finally perform pulse compression. The pulse replica must account for the bistatic motion of the target exactly; for example, the transmitted pulse's chirp slope and time support will be transformed by the Doppler upon reflection from a moving target. All such factors are accounted for during pulse compression.

2.2 Experiment Description

Each bistatic experiment was scheduled with several days lead time between the transmitters (MHR/TIRA) and the participating receiver(s). Large geostationary satellites (communications satellites) with visibility to all participating sensors were chosen for each of the experiments. Each sensor was responsible for obtaining the ephemeris of the chosen target, typically from open sources, and it was also responsible for propagating the ephemeris to the experiment time and pointing the sensor properly. For each collection, 2-3 satellites

were chosen, and the data collection duration for each object was approximately 5 minutes.

As there is no automated communication between sensors, planned recording times were determined ahead of time and controlled manually at each site. The transmitter center frequency and waveform bandwidth were also pre-determined so the receiver and recording system could be set to the appropriate bandwidth and sampling frequency. Furthermore, while many of the receivers are synchronized to highly accurate hydrogen maser clocks, GPS is the only time synchronization between the transmitter and receivers, and this was assumed to be sufficient for the purpose of these experiments.

NATO SET-293 members have conducted a number of experiments since early 2020 to establish procedures, data formats and test processing chains. The radio telescope receivers generally have multiple options for data acquisition to serve their own users. While it may be simpler to collect data in custom set-up such as an SDR receiver, many radio telescopes can record data in the vdif format (https://vlbi.org/vlbi-standards/vdif/) used for VLBI around the world. The experiments with the e-MERLIN antennas have demonstrated the processing of vdif data streams for radar applications. Table 2.2 lists the dates, the participating sensors, the NORAD ID number of the target satellites and the basic signal processing outcome of the successful experiments. Figure 2-2 show a picture of the satellites and longitudinal location. Other test experiments that did not result in target measurements are not included. For each of the target satellites, historical monostatic RCS measurements from MHR were used for comparison to the measured mono- and bistatic RCS during the experiment.

Table 2-2 – Experiment dates, sensors, objects and the basic processing outcome of each experiment conducted

Date	Sensors	Objects	Outcome
Jan 2020	MHR-WSRT	43039 27683	RCS Measurements
Mar 2021	MHR-SRT	43039 42950 41036	RCS Measurements
Feb/May 2021	MHR-e-MERLIN	43039 42950 27683	Target Detection
May 2021	TIRA-JBO	43039 37775	Target Detection, range-rate analysis and RCS measurements

Fig. 2-2 – Depictions and locations of the 5 Geostationary communications satellites referred in Table 2-2 used as collection targets for the bistatic experiments. The Astra 1N (37775) satellite is part of a GEO cluster of 4 closely spaced RSOs.

3.0 EXPERIMENT RESULTS

3.1 Results for MHR transmitting

Each bistatic data recording consisted of raw A/D samples, recorded with either real or I/Q sampling. The targets' ephemerides were used to predict the location of the pulse samples in the recorded data stream, then we extracted the samples and performed pulse compression. The pulses were then divided into 512 pulse (10s) coherent processing intervals (CPIs) and arranged into range-time intensity plots (RTIs). In some data sets, the target was visually detectable in the RTI, but in others it was very faint. Next, the pulses were coherently integrated to form range-Doppler maps, at which point all experiments had enough sensitivity to perform detection processing and measure the target SNRs in each CPI. Each data set produced 20–25 ten second CPIs, once the transmitter and receiver data sets were time aligned. Note that the 0th range and Doppler bin correspond to the predicted range and Doppler, respectively, so all ranges and Dopplers are relative to this origin.

Figures 3-1a and 3-1b depict the range-time intensity plots produced from the signals received at WSRT for objects 43039 and 27683 (January 2020). Figures 3-1c and 3-1d show the corresponding range-Doppler maps. These plots show a single CPI of the left-hand circular polarization channel recorded at WSRT.

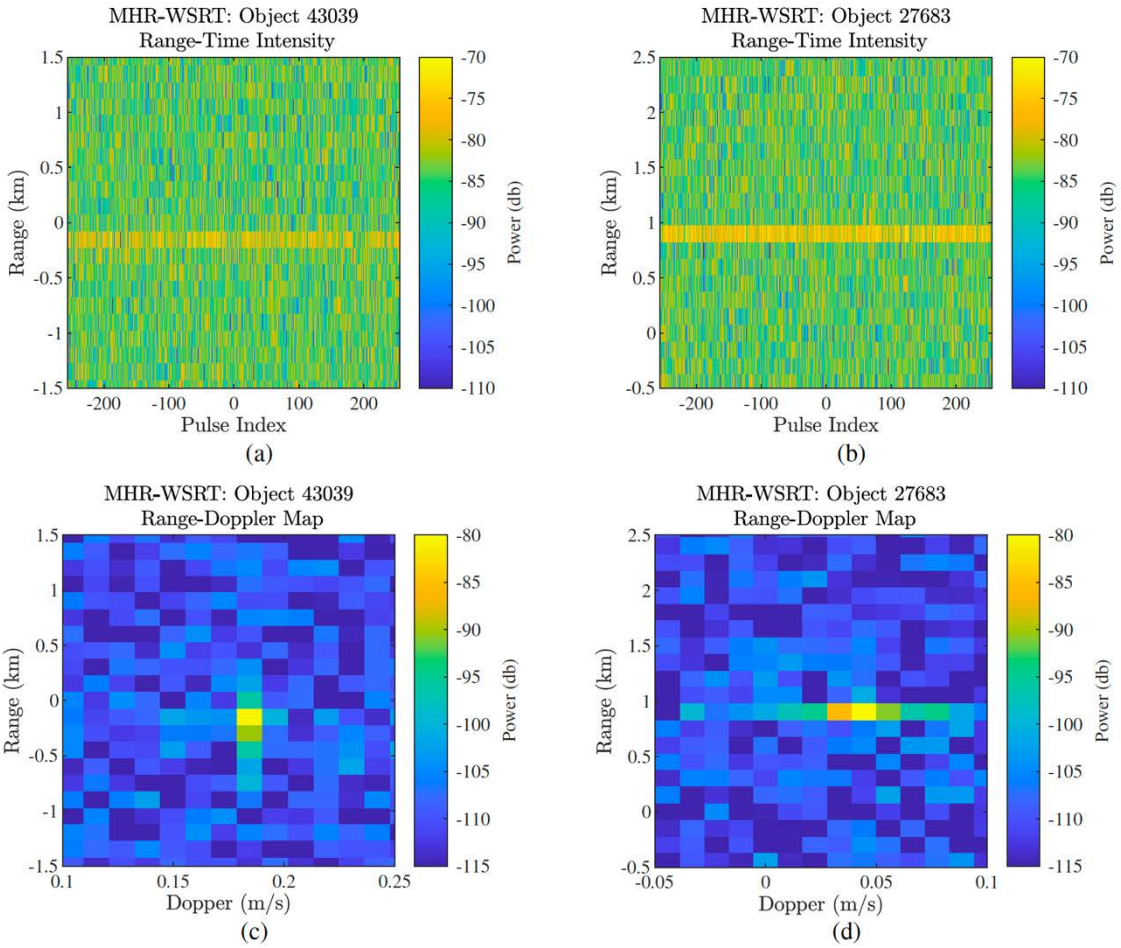

Fig. 3-1 – MHR to WSRT bistatic Range-Time Intensities and Range-Doppler Maps for objects 43039 and 27683

Although all known target motion and time delays are accounted for during processing, there is still an observable range bias and Doppler shift in the resulting plots. As a known bias example, some sensors have a known cable delay such that the time that the energy is incident on the sensor has a known bias from the recorded sample time. These known biases are accounted for as much as possible. Ideally, the target would appear at (0,0) relative range and Doppler since the origin of the range-Doppler maps correspond to the expected target range and Doppler.

There are multiple factors that could contribute to the range bias, such as TLE error and timing differences between the transmit and receive site clocks. Both of these types of errors will result in the target appearing in a different position than the TLE predicted, and a timing bias is indistinguishable from a TLE range bias. The Doppler offset is similarly hard to attribute. If the exact bistatic Doppler of the target is not matched during pulse compression, then a phase ramp will remain across the pulses, causing a Doppler offset. A Doppler offset, however, does not affect the coherence of the pulses, so reliable measurements are possible.

No non-linear time-varying delays nor any Doppler defocusing that would result from target acceleration mis-match and create a quadratic phase error across the pulses were observed. Note that the Doppler errors induced by any bistatic mismatch could also be ambiguous over the PRF. However, as the measured Doppler error appears quite small, and the range rate determined from range measurement over several minutes is similarly small, this appears not to be the case. To confirm the coherence of the pulses and the lack of Doppler defocusing, the pulses were integrated for increasingly longer CPIs and the expected increase in

target SNR, i.e. for each doubling of CPI length an additional 3 dB of SNR is gained, was observed. Figure 3-2 shows the measured SNRs at both MHR (monostatic) and WSRT (bistatic) as a function of CPI length. The maximum integration time tested was approximately 80 seconds, or 4096 pulses. Each plotted SNR is the median value taken across as many non-overlapping CPIs as could be processed from the dataset. Similar results were observed for the SRT datasets.

3.1.1 Extended coherent integration

The MHR-WSRT data was processed initially at MIT LL, and then at TNO, with very similar results. Although minor differences are still under investigation, the overall results were confirmed by this second round of data processing. In addition, longer integration times were examined, up to the maximum time available, which was about 240 seconds as observed in Figure 3-3. A drop in coherent gain was observed between 80 and 100 seconds, and dropping completely beyond 100 seconds. At the same time a blurring of the Doppler response was noted. This is consistent with a quadratic phase error. Since a high SNR was already obtained with limited integration time, the phase error could be estimated which indeed showed a dominant quadratic component. As expected, compensating this component did indeed restore the full coherent gain. From the limited data set definite conclusions as to the source of this error could not be made. Possible sources are uncompensated acceleration (order 10^{-4} m/s), frequency drift between transmitter and receiver (order 10^{-4} ppm), and possibly other time- or frequency mismatches in the bistatic setup or -processing. Additional measurements are needed to discriminate between sources of error, e.g. to distinguish between motion induced errors and errors resulting from mismatches in the bistatic setup. Systematic bistatic mismatches are expected to impact different objects in a similar way; while phase error estimation at high SNR is very well possible, identifying and compensating systematic errors could allow detection of much weaker targets, where very long integration times may be needed. Further processing for longer integration times at MHR are planned.

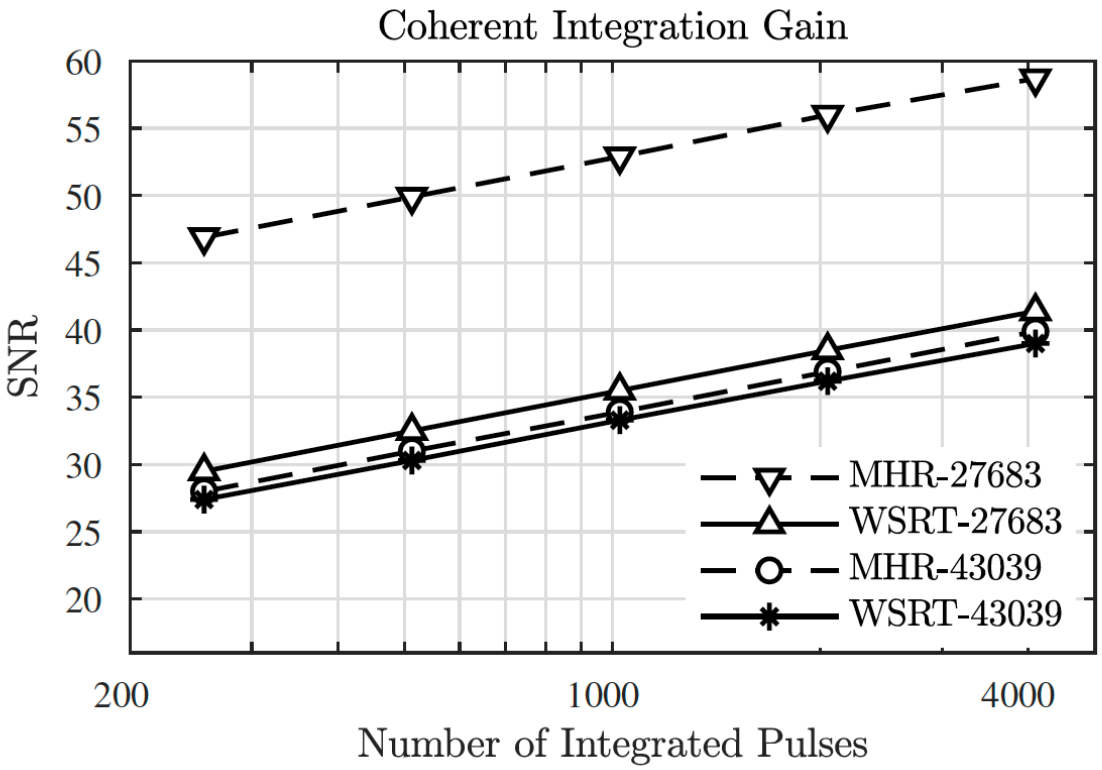

Fig. 3-2 – Coherent integration gain as a function of increasing integration (number of pulses over time). The expected coherent gain (3 dB) is observed for each doubling of the integration time. The MHR Pulse Repetition Frequency (PRF) was approximately 50 Hz yielding a total integration time of about 80 seconds for the above results.

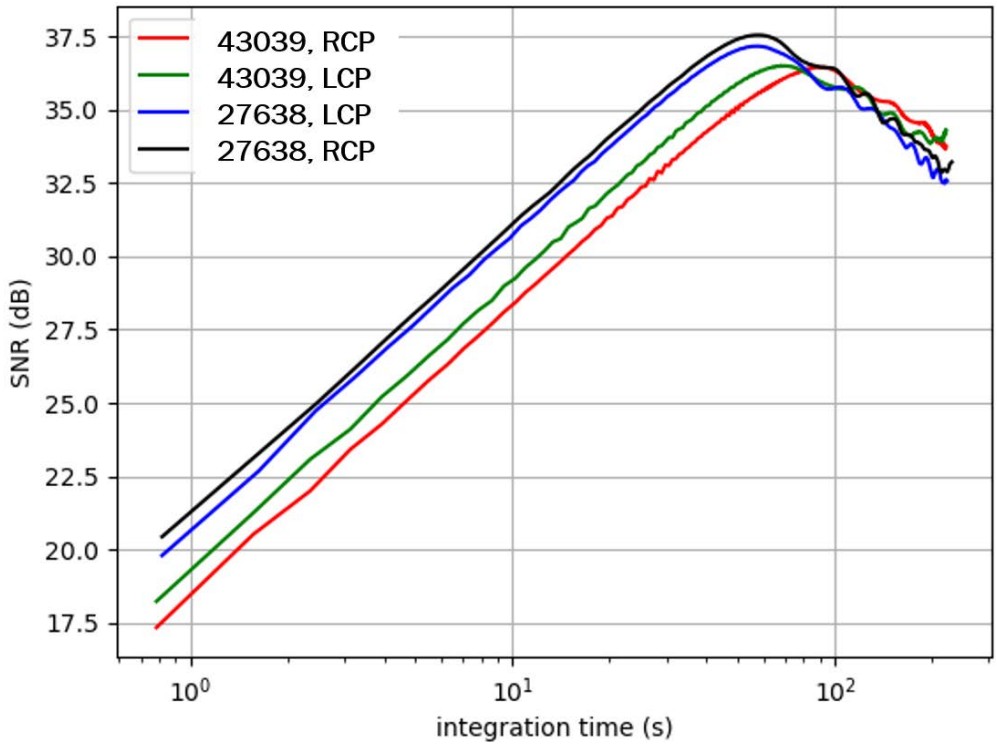

Fig. 3-3 Coherent integration gain as a function of increasing integration (number of pulses over time) time for two polarizations, which were measured sequentially. The expected coherent gain (3 dB) is observed for each doubling of the integration time up to approximately 70 seconds, where a fall in coherent gain is seen.

The phase errors estimated from the data sets shown in Figure 3-3 are shown in Fig 3-4. There is a dominant quadratic component and small remaining higher order errors. By removing the quadratic phase error, focus and coherent gain are restored.

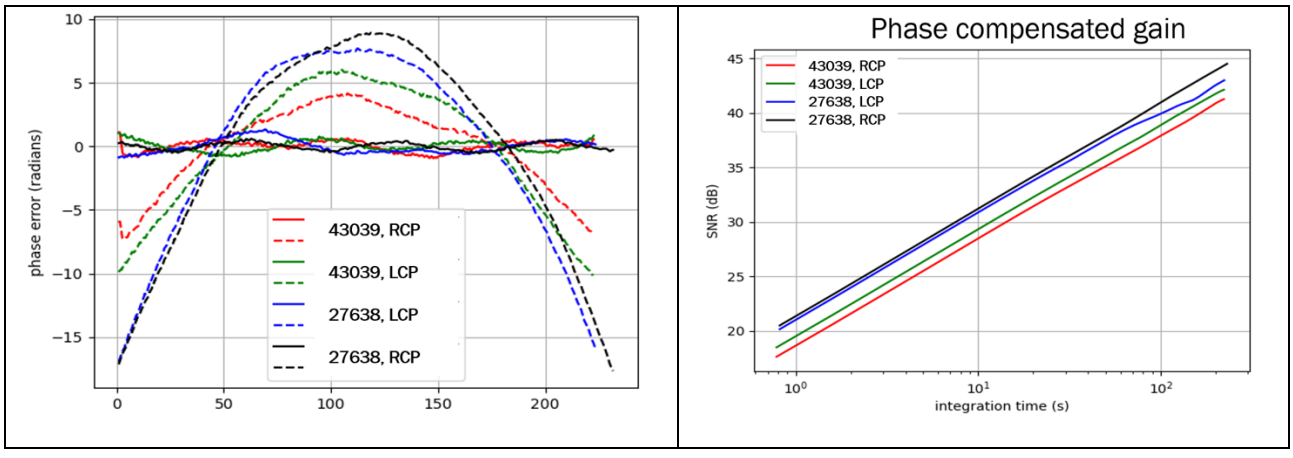

Fig. 3-4 Estimated phase error (left) and coherent gain after compensation (right). The actual phase error minus a linear fit is shown with dashed lines, the error minus a quadratic fit is shown with solid lines.

Tables 3.1 and 3.2 show the full results from the bistatic data collected at SRT and WSRT. Once again, the median values listed in the tables are computed from the values measured in as many 512 pulse CPIs as each dataset contained. Rather than show the absolute SNR measurement at each receiver, the difference between the simultaneous monostatic SNR and the bistatic SNR (i.e. SRT minus MHR) is listed to summarize the bistatic gain more succinctly. These SNR gains can then be directly compared to the last row of Table 2.1 which shows the expected receiver gain under the assumption of a constant RCS.

One potential issue is the lack of a common calibration object which is needed to accurately map SNR to RCS. For monostatic radar, this is achieved by measuring the SNR on a near-earth calibration sphere of known radius, but there are no orbiting calibration spheres with simultaneous visibility to all sensors in this bistatic geometry. As such, we are limited to measuring the SNR in the bistatic data and then computing what RCS would produce such an SNR based on the known sensor parameters. Tables 3.1 and 3.2 also list the median RCS values computed from the measured SNRs for both the bistatic and monostatic data as well as the typical range of RCSs that MHR has historically measured for the given objects.

The results show that the bistatic RCS is both lower than the monostatic RCS, but also far more variable on a per object basis. Object 43039 had a very similar bistatic RCS at WSRT and SRT, which lends hope that a particular object's bistatic RCS may be fairly constant at similar geometries, but ultimately more data is needed to confirm this result.

Table 3-1 – Experiment results between MHR and the 64 m SRT. The baseline is 6500 km with a 10 degree bistatic angle.

SRT and MHR: SNR and RCS Measurements			
Object	43039	42950	41036
Median SNR Gain at SRT (dB)	4.3	3.1	-15.3
Median SRT RCS (dBsm)	11.6	15.2	-5.1
Median MHR RCS (dBsm)	22.9	28.0	26.0
Historical MHR RCS (min,max)	(22,23)	(27,28)	(24,25)

Table 3-2 – Experiment results between MHR and a single WSRT antenna. The baseline is 5700 km with a 9 degree bistatic angle.

WSRT and MHR: SNR and RCS Measurements		
Object	43039	27683
Median SNR Gain at WSRT (dB)	0.6	-17.4

Median WSRT RCS (dBsm)	12.6	14.6
Median MHR RCS (dBsm)	19.4	38.2
Historical MHR RCS (min,max)	(22,23)	(39,40)

3.2 Results for TIRA transmitting

TIRA used a non-modulated waveform with a pulse length of 1 millisecond yielding a range resolution of 150 km and a range rate resolution of 112 m/s. A list of beam crossing objects was compiled from the TLE catalogue downloaded from Space-Track. The list took into account only objects that were both located in the antenna beam and in the same range/Doppler cell as the observed objects after matched filtering. In particular for the observation of object 37775, a total number of six GEO satellites were illuminated by the radar antenna; two of them being at the edges of the antenna beam. Therefore, the signals backscattered by four satellites were expected to be detectable in the receive data after matched filtering.

3.2.1 Monostatic Results

In order to discriminate and detect these objects, the data were coherently processed [8]. Figure 3-5 shows the result after integration over 251 pulses corresponding to a CPI of about 8 s and a processing gain of about 24 dB. Four satellites can be clearly discriminated in Figure 3-5a. After applying a CLEAN-like detection over the different CPIs, the range rates of the different satellites can be plotted over the observation time (Figure 3-5b). After correlation with the TLE catalogue, the different detections can be attributed to four GEO satellites.

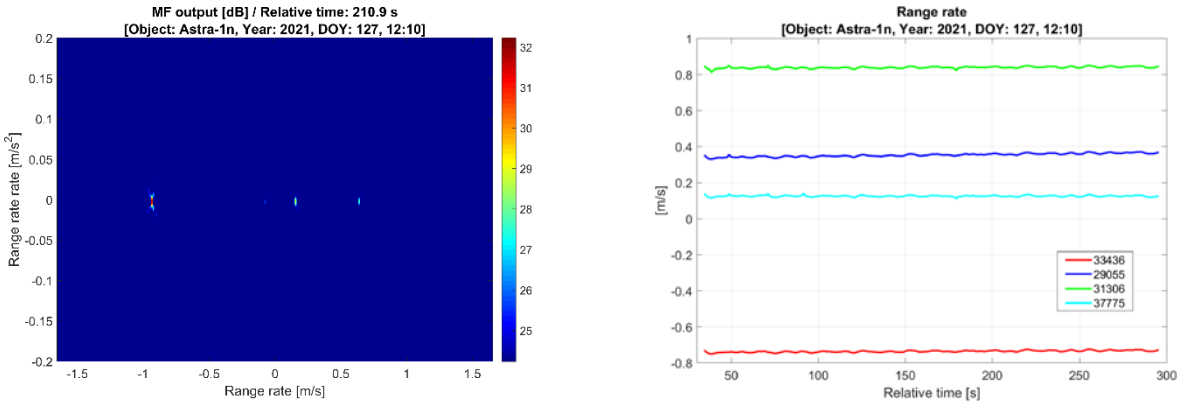

a) Result after coherent integration **b) Estimated range rate over time**

Fig. 3-5 – Coherent integration results for TIRA monostatic measurements from the May 2021 experiment.

As discussed previously, the RCS of an object is a major parameter for its detectability with a radar. The RCS depends on many parameters such as the used radar frequency, the polarization, the object material and shape, and the incidence angle. In May 2021, the object 43039 was illuminated by MHR and TIRA almost simultaneously. The TIRA system measured a RCS of 29 dBsm, about 6 dBsm higher than MHR indicating a high directionality of the monostatic RCS for the observed object.

3.2.2 Bistatic Results

In the same observation three antennas (Knockin 25m, Pickmere: 25m and Cambridge: 32m) of the e-MERLIN array were used simultaneously to receive the TIRA signal at 1.33 GHz in both RCP and LCP. The antennas have relative separations of 60 to 220km; the data are sent on a dedicated optical link to Jodrell Bank at full bandwidth (500 MHz) where the e-MERLIN correlator was used to extract multiple sub-bands, with a 2 MHz sub-band centered on the TIRA signal. The data were recorded in vdif format and independently processed at JBO and DSTL. The high SNR of object 37775 and its neighbors along with the simple unmodulated TIRA narrow-band waveform allowed the pulse train and even individual pulses to be detected on all three antennas with straightforward FFT processing. Figure 3.6a shows pulses received with the 34.0 ms PRI. Given the relatively short bistatic baselines (520-740km) there initially was concern that the signal could be via anomalous propagation over the ground, even though the reflected signal should be stronger. Subsequent analysis leaves no doubt that the reflected signal was detected and there was no sign of signals in very different range bins.

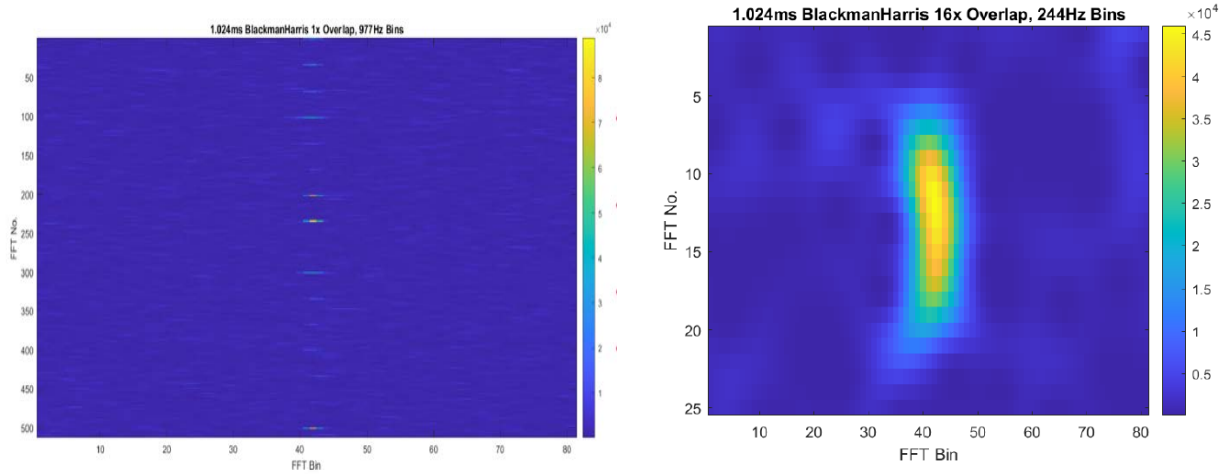

Figure 3.6 (a) Pulse train received at Knockin antenna with consecutive FFTs and 1.024ms time resolution; (b) spectrogram of a single pulse, 244 Hz frequency bins, 1.024 ms FFTs with 16x overlap

Figure 3.6b shows a single pulse recovered at high time resolution and with high SNR. Range-Doppler analysis was carried out independently at JBO and Dstl and all 4 targets which were detected in the monostatic TIRA analysis were detected at all 3 antennas. Given the low expected range rates, a simple pulse compression scheme (pulse length 1.0 ms, period 34.0 ms) with no Doppler correction was used. There were significant differences in SNR observed at the different receiving antennas, even between the four targets, which may be result of small pointing errors given that the separation of the objects on the sky is a significant fraction of the telescope beamwidth. The highest SNR was achieved on the 25-m Knockin telescope and the analysis presented here concentrates on those data.

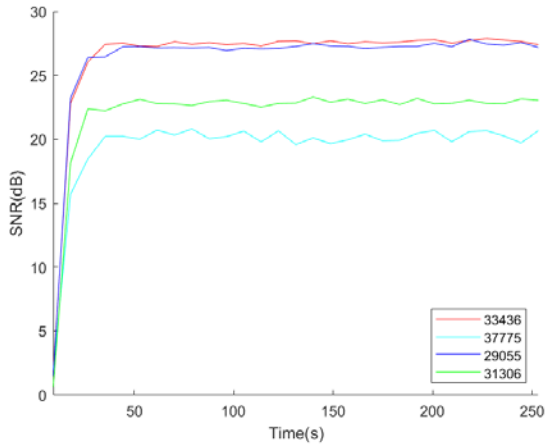

Figure 3.7 SNR versus time after Range-Doppler analysis for the four targets in the TIRA-Knockin bistatic data with 256 pulses integrated per CPI

Figure 3.7 shows the SNR versus time for the four objects after Range-Doppler processing using a 256-pulse PRI. Figure 3.8 shows that the SNR increases by 3dB for each doubling of the number of integrated pulses up to 1024 pulses (35 seconds) for all four objects. When integrating over a CPI of 2048 pulses (70 seconds) two of the objects, 33436 and 31306, show a further 3dB coherent gain. There are two anomalous points, for objects 29055 and 37775, which are still under investigation.

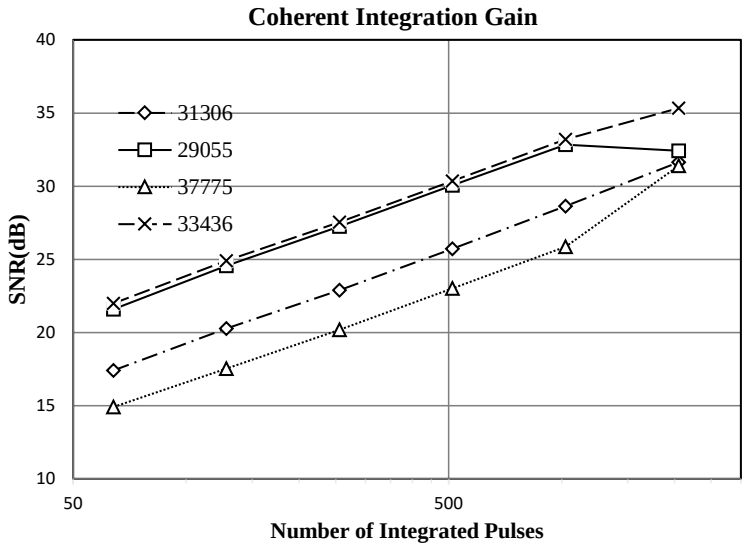

Figure 3.8 SNR results from coherent Range-Doppler analysis for the TIRA-Knockin bistatic data versus number of integrated pulses

Figure 3.9 shows the range rate map for a single 512-pulse CPI (as used in the monostatic case) and the range profiles for the four targets showing small offsets and Figure 3.10 shows the range rates and their fitted slopes vs time. [Comments on comparison between monostatic and bistatic range rates]. Although these observations with a simple unmodulated pulse were not designed to have high range resolution, the range differences of the four objects are just visible.

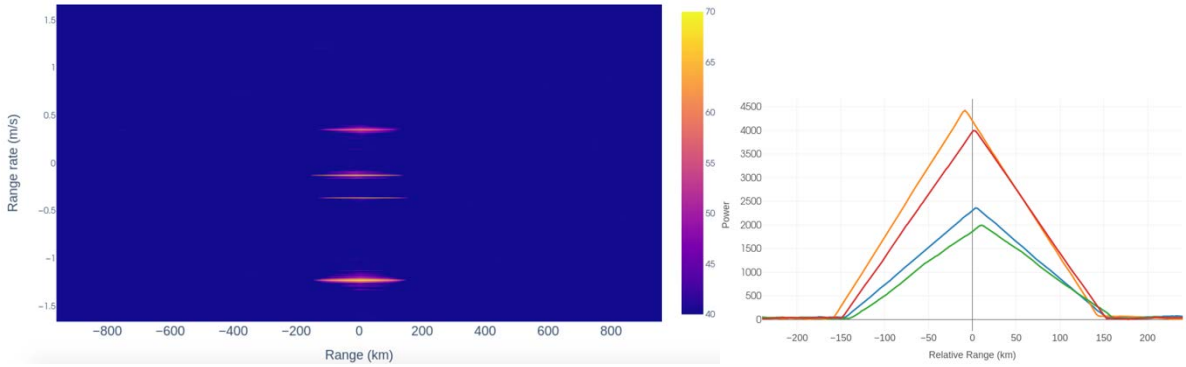

Fig 3.9 (a) Range-rate map for the TIRA-Knockin bistatic data using a CPI of 512 pulses (b) range profiles of the four targets after pulse compression.

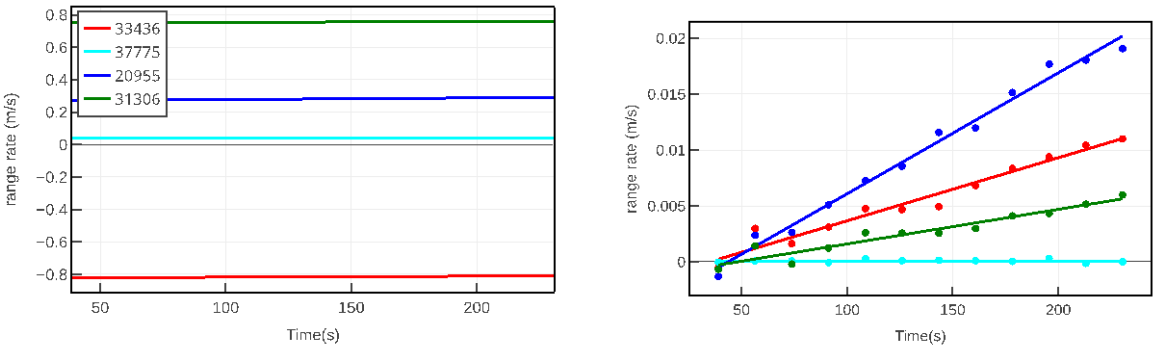

Fig 3.10 (a) Range rates from the TIRA-Knockin bistatic data. The overall rates have been offset to match Fig 3.5b. (b) As (a) but zoomed in the y-axis with the four targets offset in rate to show the different rate slopes.

For each object there are small but discernible range and rate differences between the receiving telescopes which are broadly consistent with the expectations from the TLE target velocities and antenna positions. In principle, these differences can be inputs for a multilateration solution for the target state vectors. In addition to using the measured range and rate differences of the signals measured separately using pulse compression independently at each antenna, it is also possible to do a direct cross correlation of the signals from each of the receiving antennas (as is normally done for radio astronomy and VLBI geodesy). In effect this cross correlation can replace the pulse compression using the modified model transmitter pulse waveform. The signal is indeed detectable in the cross-correlations and there may be potential advantages in using this technique to augment the normal pulse compression approach; further results will be presented at a later stage.

4.0 CONCLUSIONS

Successful continental baseline coherent bistatic radar collections on GEO targets have been demonstrated. Current results show that one can coherently integrate the bistatic pulses and determine the bistatic RCS. Further, Range-Doppler processing enables, not only focused detection, but also multi-target detection when more than one satellite is in the receive beam. This is seen in the May 2021 experiment which include

observations of a GEO cluster in which all 4 objects seen in the monostatic data are detected on multiple telescopes in the bistatic data. Further data collections on a wider variety of objects, including multiple objects in the receive beams will confirm these capabilities. In addition, new experiments will incorporate astronomical calibration of the instrumental and propagation delays and phase rates in order to improve accuracy and to increase the coherence time between different receive antennas. Bistatic radar, especially with large, highly sensitive radio telescopes remains a promising and low-cost way to achieve increased sensitivity. Additional data collections have already been conducted in 2022 under the NATO SET-293 effort and analysis is in process. Further, there are plans to incorporate a new X-band receiver in the UK enabling new bistatic collections with the high power HUSIR X-band radar operated by MIT Lincoln Laboratory (USA).

ACKNOWLEDGMENT

The authors also wish to acknowledge the NATO Sensors, Electronics and Technology Research Technology Group (RTG) and the United States Space Command for sponsoring this research. e-MERLIN is operated by the University of Manchester on behalf of UK Research and Innovation and has received funding from the European Union's Horizon 2020 research and innovation programme under grant agreement No 101004719

REFERENCES

[1] D. DeBoer and D. Bock, "The allen telescope array: splitting the aperture," IEEE Microwave Magazine, vol. 5, no. 2, pp. 46–53, 2004.

[2] Duev, D, Molera-Calves, G, Pogrobenko, S et al (2012) Atronomy & Astrophysics, Volume 541, 43.

[3] N. Willis, Bistatic Radar. Boston, London: Artech House, 1991.

[4] Lincoln Laboratory, Massachusetts Institute of Technology. (2022) Lincoln Space Surveillance Complex. [Online]. Available: https://www.ll.mit.edu/about/facilities/lincoln-space-surveillance-complex

[5] M. Richards, Fundamentals Of Radar Signal Processing. New York, NY: McGraw-Hill, 2005, ch. 4.

[6] C. V. Jakowatz, D. E. Wahl, P. H. Eichel, D. C. Ghiglia, and P. A. Thompson, Spotlight-Mode Synthetic Aperture Radar: A Signal Processing Approach. Boston, MA: Springer US, 1996, pp. 1–31.

[7] K. Letsch, L. Leushacke1, J. Rosebrock1, R. Jehn, H. Krag, and R. Keller, First Results from the Multibeam Bistatic Beampark Experiment at FGAN, 5th European Conference on Space Debris, 2009

[8] D. Mehrholz, Radar Observations of Geosynchronous Orbits, 2nd European Conference on Space Debris, 1997

[9] D. Cerutti-Maori, J. Rosebrock, C. Carloni, M. Budoni, I. Maouloud, and J. Klare, A Novel High-Precision Observation Mode for the Tracking and Imaging Radar TIRA – Principle and Performance Evaluation –, 8nd European Co1nference on Space Debris, 2021